





Dynamics of a laser-induced buoyant bubble near a vertical rigid boundaryPeng Xu ¹, Bo Li ^{1,2}, Zibo Ren ¹, Shuhong Liu,^{1,*} and Zhigang Zuo ^{1,†}¹State Key Laboratory of Hydrosience and Engineering, and Department of Energy and Power Engineering, Tsinghua University, Beijing 100084, China²Beijing Key Laboratory of Information Service Engineering, Beijing Union University, Beijing 100101, China

(Received 14 February 2023; accepted 12 July 2023; published 2 August 2023)

In this paper, systematical experiments are carried out to study the distinct behavior of a buoyant cavitation bubble near a vertical rigid boundary. Under the combined influence of gravity and the rigid boundary, the bubble centroid migrates rapidly when the bubble completely collapses, and a microjet of intermediate strength subsequently penetrates the bubble in the same inclined direction. By recalling the nondimensional form of the Kelvin impulses, or the pressure anisotropy parameters, we analytically predict the angle between the jet and the horizontal direction at different experimental conditions. We further successfully establish the scaling law of the jet velocity by denoting the displacement of the bubble centroid as the characteristic length scale. The findings of this study contribute to our understanding of the nonspherical cavitation bubble dynamics under the simultaneous influence of multiple factors.

DOI: [10.1103/PhysRevFluids.8.083601](https://doi.org/10.1103/PhysRevFluids.8.083601)**I. INTRODUCTION**

In engineering where cavitation occurs, the pressure around the individual cavitation bubble is usually nonuniformly distributed due to the presence of adjacent interfaces (such as rigid boundaries, free surfaces, and two-fluid interfaces), as well as the flows and the body forces [1–3]. As a result, each point on the bubble interface moves at different speeds, particularly when it collapses. The bubble then experiences a nonspherical collapse, characterized by its nonspherical deformation, bubble centroid migration, and microjet formation.

For example, a rigid boundary or a free surface near a cavitation bubble causes the bubble to deform nonuniformly. The pressure gradient ∇p around the bubble in these cases is *self-generated*, in the sense that it arises from the flow by the bubble-induced point source near the boundary/free surface [2]. Without the movement of the bubble interface, there would be no such pressure gradient. The physical boundary nearby eventually induces migration of the bubble centroid and a liquid microjet toward the boundary or away from the free surface during the collapsing period if the effect is strong enough. When this effect becomes weaker, the bubble remains spherical during most of its lifetime from its inception to its first collapse. Instead, the migration of the bubble and the formation of the jet are observed during subsequent bubble rebound [4,5]. The strength of this effect is measured by a nondimensional standoff distance γ of the bubble centroid against the boundary/free surface. Generally, the effect of a single interface on the cavitation bubble decreases with increasing γ , and is considered negligible if $\gamma > 5$ [1].

In addition to different forms of physical boundaries, gravity (i.e., buoyancy) is a typical example of body force that gives rise to the pressure gradients in the liquid, leading to the nonspherical

*liushuhong@mail.tsinghua.edu.cn

†zhigang200@mail.tsinghua.edu.cn

collapse of the cavitation bubble. The pressure gradient caused by gravity can be simply expressed as $\nabla p = \rho \mathbf{g}$ and is constant in the liquid domain when \mathbf{g} is known, which is different from that caused by the physical boundaries. It is known that the strength of the effect of gravity is dependent on the maximum bubble size and the ambient pressure. Under atmospheric pressure ($p_\infty = 1$ bar), this influence is difficult to detect for a bubble with $O(R_{\max}) \leq 1$ mm [2,6], while in the case of large bubbles such as underwater explosions, the gravity effect cannot be ignored. Furthermore, in rotating fluid machinery, the centrifugal force plays a similar role as gravity, but of much larger magnitudes [7].

In order to quantify the nonspherical collapsing characteristics of a cavitation bubble under the influence of the pressure gradients, Supponen *et al.* [1] introduced an anisotropy parameter ζ , which is essentially a dimensionless form of the Kelvin impulse. For different pressure-gradient generators, such as rigid boundary, free surface, or gravity, ζ has different expressions. The strength of the jets at bubble collapses can then be defined and described by the values of ζ . In general, when ζ is large (e.g., $\zeta > 0.1$), the bubble undergoes significant deformation and the jet penetrates the opposite side of the bubble interface prior to collapse, a phenomenon referred to as a *strong jet*. Current studies on nonspherical cavitation bubble dynamics primarily concentrate on the strong jet regime. For smaller ζ values (e.g., $0.001 < \zeta < 0.1$), a less intense *intermediate jet* does not pierce the bubble until its collapse is complete. This jet can only be detected during the rebound stage and is more complex and challenging to quantify.

A number of research studies have also focused on the combined effect of multiple factors acting simultaneously. Blake and Gibson [4] and Brujan *et al.* [8] studied cases where a buoyant bubble collapses above a horizontal rigid wall. Three different behaviors of the collapsing bubble have been identified, according to the direction of the jet, namely the upward jet, the downward jet, and the neutral collapse, based on the numerical simulations through the boundary-integral method. Then the concept of a Kelvin impulse has been successfully applied to establish the conditions for different jet directions. In a subsequent study, the experimental results of Zhang *et al.* [9] support the relevant findings. Notice that the effects of gravity and the horizontal wall are parallel but in opposite directions in these cases. In contrast, Tagawa and Peters [10] have studied the bubble collapses in the corner of two perpendicular walls. Based on the method of images, they have discovered that the directions of the bubble migration and the inclined jet are solely the functions of the ratio between the distances from the bubble to the two boundaries. Wang *et al.* [11] also used the method of images in their numerical investigation of a bubble collapsing at a corner geometry. The numerical results revealed the structure of the *strong jet* that forms prior to the bubble's complete collapse. Nonetheless, the simultaneous influences of both gravity and a boundary that are not parallel to each other are still not well understood. Since the pressure gradients resulting from rigid boundaries and gravity have distinct dependencies on the flows induced by the bubble, in contrast to the bubble dynamics near two rigid boundaries, the method of images cannot be used to evaluate the impact of gravity when the influences of both a rigid boundary and gravity are simultaneously considered. In experiments, it is difficult to highlight the influence of gravity on a millimeter-scale bubble under atmospheric pressure, and the analytical approaches described in the previous literature also need validation for this particular purpose [12,13].

In this paper, we generate large laser-induced cavitation bubbles (the maximum radius R_{\max} reaches about 6 mm) by lowering the background pressure in a sealed water tank, thus making the effect of gravity more pronounced. Meanwhile, we introduce a vertical rigid boundary near the bubble. Driven by both gravity and rigid boundary, the directions of the bubble migration and the intermediate jet deviate from the vertical direction. The variation of the angle between the jet and the horizontal direction, and the jet velocity characterized by the nondimensional transient migration velocity of the bubble centroid during the final bubble collapse, are summarized through high-speed images of the bubble dynamics. Then by recalling the nondimensional form of the Kelvin impulse, or the pressure anisotropy parameters, we analytically predict the jet angle and successfully establish the scaling law of the jet velocity. The results of this research provide additional information

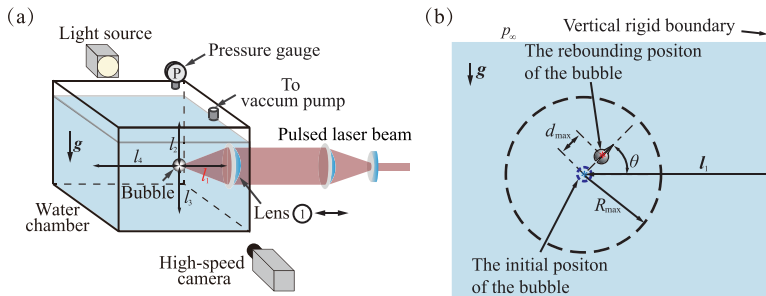


FIG. 1. Configurations of the experiments. (a) Schematic of the experimental setup synchronized with the laser pulse and (b) experimental notation. The inner sidewall of the chamber through which the laser beam enters serves as the rigid boundary in the vicinity of the cavitation bubble.

on the nonspherical cavitation bubble dynamics under the simultaneous influence of multiple factors.

II. EXPERIMENTAL SETUP

As schematically shown in Fig. 1(a), a cavitation bubble is induced by focusing a pulsed Q -switched ruby laser (QSR9, Innolas Ltd., U.K.) into degassed water in a rectangular transparent plexiglass water chamber that is 280 mm in length, 200 mm in width, and 200 mm in depth. Since the effect of gravity is not enough to produce visible deformations and jets for a cavitation bubble with a maximum radius $R_{\max} \lesssim 2$ mm under atmospheric pressure [1], we produce relatively large bubbles with $R_{\max} = 2.6\text{--}6.5$ mm in experiments by reducing the background pressure ($p_{\infty, \min} = 8476$ Pa) through a vacuum pump (Rocker400, Rocan Scientific Company, Ltd., Taiwan, China). The pressure in the tank is recorded with a pressure gauge (PT3081, Shanghai Hengrui Measurement and Control Technology Company, Ltd, China) with a full-scale (FS) precision of 0.5%.

The desired nondimensional standoff distance of the bubble against the vertical sidewall $\gamma = l_1/R_{\max} = 2.38\text{--}13.80$ is realized by adjusting the horizontal position of the convex lens (① in Fig. 1). The effects of the free surface and other boundaries on the dynamics of the bubble can be neglected, with $l_2/R_{\max} \geq 15$, $l_3/R_{\max} \geq 15$, and $l_4/R_{\max} \geq 30$. The behavior of the cavitation bubble under the combined influence of both gravity and the solid boundary nearby is then recorded by a high-speed camera (Phantom V711, Vision Research Inc., U.S.A.) at a frame rate of 48 022 fps with a spatial resolution of $116.9 \mu\text{m}/\text{pixel}$. The radius of the cavitation bubble R , and the distance from the center of the bubble to the vertical wall l_1 , are measured directly from the calibrated images, with the uncertainty of 1 pixel. As the bubble collapses, an inclined microjet forms under the combined effects of the solid boundary and gravity, as schematically shown in Fig. 1(b). The direction of the jet is identified by the maximum displacement of the bubble d_{\max} from its growth to the first rebound [10] and is defined by θ with respect to the normal of the solid boundary, i.e., the horizontal direction. The uncertainty of the measurement of θ is less than 2.5° .

III. DIRECTION OF THE JET

It is known that cavitation erosion of the solid materials is largely attributed to the microjet impacts on the boundary wall at the nonspherical bubble collapses nearby. Therefore, the direction of the jet is of great interest. In cases where influence factors besides the boundary come into play, e.g., flows [14], multiple interfaces [6, 10, 15], and the buoyancy force [12], the direction of the jet is influenced by their combined effects.

Figure 2 shows examples of high-speed images of the collapse and rebound of cavitation bubbles under the influence of pressure anisotropy induced by the combined effects of gravity and a vertical

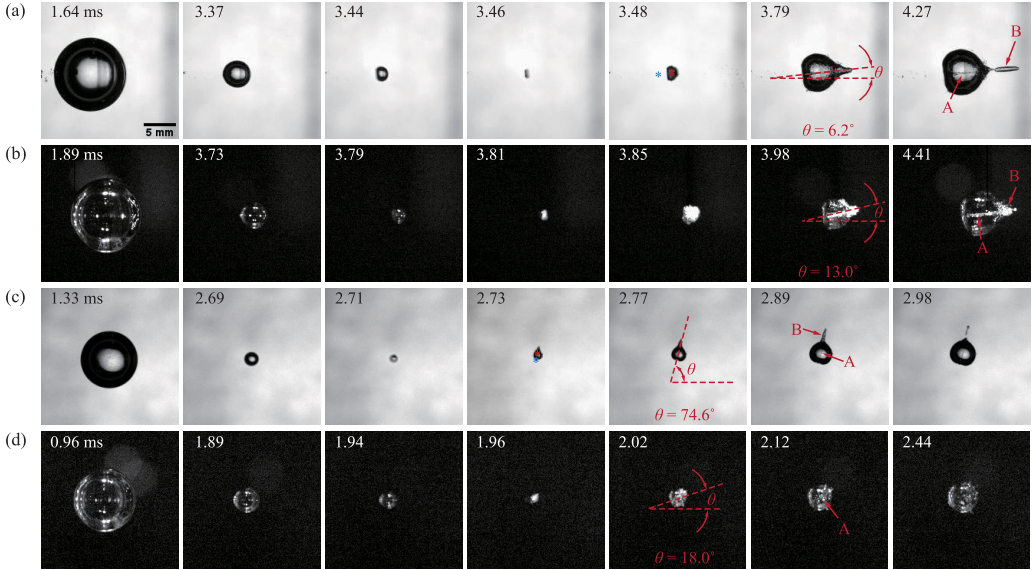


FIG. 2. High-speed images of the collapse and rebound of cavitation bubbles under the influence of pressure anisotropy induced by the combined effects of gravity and a vertical rigid boundary: (a) $R_{\max} = 5.62$ mm, $\Delta p = 8441.3$ Pa, $l_1 = 17.00$ mm ($\zeta_g = 0.0048$, $\zeta_w = 0.0213$, $\zeta = \sqrt{\zeta_g^2 + \zeta_w^2} = 0.0218$); (b) $R_{\max} = 5.50$ mm, $\Delta p = 7011.4$ Pa, $l_1 = 19.06$ mm ($\zeta_g = 0.0061$, $\zeta_w = 0.0162$, $\zeta = 0.0173$); (c) $R_{\max} = 4.37$ mm, $\Delta p = 8613.2$ Pa, $l_1 = 60.31$ mm ($\zeta_g = 0.0049$, $\zeta_w = 0.0010$, $\zeta = 0.0050$); (d) $R_{\max} = 4.74$ mm, $\Delta p = 20186.2$ Pa, $l_1 = 32.28$ mm ($\zeta_g = 0.0011$, $\zeta_w = 0.0042$, $\zeta = 0.0043$). Cases (a) and (c) are recorded with back illumination, and cases (b) and (d) are recorded with front illumination. The liquid jets at bubble collapses are indicated by “A,” and the thin vapor layers around the jets are indicated by “B.” The initial position of the bubble center at $t = 0$ is marked with a blue “*,” and the position of the bubble center at $t = 1.01T_c$ is marked with a red “*,” where T_c is the lifetime of the cavitation bubble from growth to its first collapse.

rigid boundary. In order to show the inner structures of the bubbles, a number of experiments are performed using front illumination, as exemplified in Figs. 2(b) and 2(d). The first frame in each row of Fig. 2 indicates the maximum bubble size, where the bubbles still remain spherical. For the cases shown in Figs. 2(a) and 2(b) (see Supplemental Movies 1 and 2 [16]), the sphericity of the bubbles is broken as they fold on themselves near the end of their collapses, as indicated in their third frames. The bubbles are then pierced by thin inclined liquid jets during rebounds. In contrast, for the cases shown in Figs. 2(c) and 2(d) (see Supplemental Movies 3 and 4 [16]), no obvious nonspherical deformation is observed until the bubbles reach the minimum sizes, and then the jets form almost instantly. Particularly, in Fig. 2(d), the influence of nonuniform factors on the bubble is even weaker, and the jet barely penetrates the cavitation bubble during the rebound stage. The existence of the jet can only be proven by observing the interior of the bubble. In Fig. 2, the liquid jets are indicated by “A” for each case. It is seen that the shape and time of occurrence of the jets are generally consistent with *intermediate jets* described in Refs. [1,17]. The inclinations of the jets are characterized by the angles of the jets θ defined in Fig. 1(b). Thin vapor layers around the liquid jets (indicated by “B”) are observed once they penetrate the opposite sides of the bubbles. Different angles θ are seen for the cases shown in Figs. 2(a)–2(d).

It is worth mentioning that in the present experimental setup, we observe the influence of the rigid boundary at unexpectedly large γ values. For example, as shown in Fig. 2(c), the jet is inclined even as γ reaches 13.8. In contrast, the influence of the boundary is usually neglected for $\gamma > 5$ when its effect on the bubble dynamics is studied separately, as described in the previous literature [1,18].

Considering the factors that result in the inclination of the jet, here we adopt the concept of a Kelvin impulse to predict θ . In an incompressible and inviscid fluid, the Kelvin impulse represents the time integral of the forces acting on the surface of the bubble during its growth and collapse [19–21]. Thus, the direction of the Kelvin impulse indicates the direction of the jet at the bubble collapse [12]. We write the Kelvin impulse accumulated by the bubble as

$$\mathbf{I} = \int_0^{T_c} \mathbf{F} dt = \int_0^{T_c} (\mathbf{F}_w + \mathbf{F}_g) dt, \quad (1)$$

where \mathbf{F} denotes the combined force applied on the bubble, including the force exerted on the bubble due to the existence of the rigid boundary \mathbf{F}_w and the buoyancy force \mathbf{F}_g , and T_c is the lifetime of the bubble from its generation to its collapse.

Ignoring the surface tension and assuming mild bubble deformation, \mathbf{F}_w could be expressed as $-\frac{\rho(4\pi R^2 \dot{R})^2 \mathbf{l}_1}{16\pi l_1^3}$, where ρ is the density of the liquid, R is the radius of the bubble, \dot{R} is the time derivative of R , and \mathbf{l}_1 is the normal vector from the rigid wall to the center of the bubble [22,23]. Using the Rayleigh equation (see Appendix A, where we verify that the evolution of the radius of the collapsing cavitation bubble under low-pressure conditions can still be described by the Rayleigh equation), the contribution of \mathbf{F}_w in \mathbf{I} is calculated as

$$\int_0^{T_c} \mathbf{F}_w dt = -\frac{5\pi}{3\sqrt{6}} B\left(\frac{5}{6}, \frac{1}{2}\right) R_{\max}^3 \sqrt{\Delta p \rho} \left(\frac{4}{5} \frac{B\left(\frac{7}{6}, \frac{3}{2}\right)}{B\left(\frac{5}{6}, \frac{1}{2}\right)} \gamma^{-2} \frac{\mathbf{l}_1}{l_1} \right) \approx 4.789 R_{\max}^3 \sqrt{\Delta p \rho} \boldsymbol{\zeta}_w, \quad (2)$$

where Δp is the pressure difference between the static pressure in the water at the level of the bubble center and the vapor pressure inside the bubble, $B(x, y)$ is the beta function, and $\boldsymbol{\zeta}_w = -\left(\frac{4}{5} \frac{B\left(\frac{7}{6}, \frac{3}{2}\right)}{B\left(\frac{5}{6}, \frac{1}{2}\right)} \gamma^{-2} \frac{\mathbf{l}_1}{l_1}\right) \approx -0.195 \gamma^{-2} \frac{\mathbf{l}_1}{l_1}$ is the nondimensional measure of the component of \mathbf{I} along the \mathbf{l}_1 direction.

Meanwhile, \mathbf{F}_g could be estimated by $-\rho \mathbf{g} \left(\frac{4}{3} \pi R^3\right)$ [24]. Similarly, we can estimate the contribution of \mathbf{F}_g in \mathbf{I} as

$$\int_0^{T_c} \mathbf{F}_g dt = \frac{5\pi}{3\sqrt{6}} B\left(\frac{5}{6}, \frac{1}{2}\right) R_{\max}^3 \sqrt{\Delta p \rho} \boldsymbol{\zeta}_g \approx 4.789 R_{\max}^3 \sqrt{\Delta p \rho} \boldsymbol{\zeta}_g, \quad (3)$$

where $\boldsymbol{\zeta}_g = -\frac{\rho \mathbf{g} R_{\max}}{\Delta p}$ is the nondimensional measure of the component of \mathbf{I} along the \mathbf{g} direction. Then the direction of the jet can be calculated by the ratio between the absolute values of $\boldsymbol{\zeta}_g$ and $\boldsymbol{\zeta}_w$ as $\tan \theta = \zeta_g / \zeta_w$.

This theoretical dependence of θ on ζ_g / ζ_w is validated, and agrees well with the experimental results, as shown in Fig. 3. The ranges of ζ_g and ζ_w are $1.1 \times 10^{-5} - 7.4 \times 10^{-3}$ and $1.3 \times 10^{-3} - 3.4 \times 10^{-2}$, respectively. In this range of the parameter space, we observe intermediate microjets when bubbles collapse. Specifically, bubbles undergo mild deformations during most of their growth and collapse. This is favorable for the estimation of the Kelvin impulses using Rayleigh solutions of spherical bubble dynamics. The deformations become significant only at the final stages of the bubble collapses, and the jets are prominent during the rebounding of the bubbles.

The formation of the jet is very sensitive to the sphericity of the bubble, especially for the *intermediate jet* occurring at the end of the bubble collapse in this study. In our experiments, the small ratio $\zeta_g / \zeta_w \ll 1$ is mainly realized by setting large ζ_w values where the bubble is produced close to the boundary. Under these conditions, the influence of the boundary is more significant, and the bubble presents a more pronounced horizontal elongation at the end of the collapse, as shown in Fig. 2(a) with an elliptical eccentricity of 0.3. The horizontally fired laser beam for bubble generation may result in a similar deformation at the bubble collapse. The flow-focusing effect induced by the nonuniform bubble curvature may contribute to the increase in the horizontal jet component [25], thus resulting in the slight downward deviation of the experimental θ from the theoretical values in this area. The direction and intensity of the microjet are very sensitive to

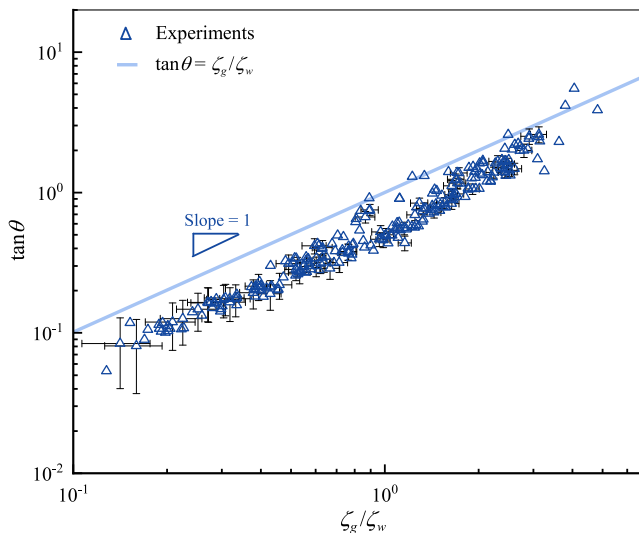


FIG. 3. Experimental validation of $\tan \theta = \zeta_g / \zeta_w$. Some measurement uncertainties are shown by the error bars.

the environment when the cavitation bubble collapses. In Appendix B we discuss in more detail the factors that may influence the jet direction and the experimental results of the laser shot from different directions.

IV. SCALING LAW OF THE JET VELOCITY

We now investigate the characteristic velocity of the jet caused by bubble collapses. As described in Sec. III, in the present experiments, the bubble starts to deform at the end of the bubble collapse, with a nonuniform velocity distribution across its surface. The fastest pole (roughly 2–3 times faster than the opposite pole) subsequently forms the jet tip. The generated *intermediate* jets can only be observed during bubble rebounds. Therefore, it is not feasible to predict the jet velocity using the maximum velocity of the *strong* jet tip before it penetrates the bubble for the present study, as in Refs. [1,9].

Based on the experimental observations that the deformation of bubble poles during bubble collapse is correlated with the jet at bubble rebound, we characterize the maximum jet velocity by the maximum migration velocity of the bubble centroid v . Note that this velocity may be underestimated due to the limited temporal and spatial resolutions of the high-speed images, but the experimental results can still provide insight into its dependence in relation to the key parameters. It has been reported in previous studies that the *strong jet* will exhibit an asymmetric structure, and its direction may deviate from that of the displacement of the bubble centroid [11,13]. In contrast, in the current experiments, the bubble maintains a spherical shape for 98% of its lifetime and its deformation is minimal, therefore the jet direction is believed to be in line with the migration direction of the bubble.

Since the jet is caused by the asymmetric forces on the bubble during its collapse, we can then present the nondimensional jet velocity $v^* = \frac{v}{\sqrt{\Delta p / \rho}}$ against ζ in Fig. 4, where $\sqrt{\Delta p / \rho}$ is the characteristic velocity of the bubble [1,26], and $\zeta = \sqrt{\zeta_g^2 + \zeta_w^2}$ is the magnitude of the combined Kelvin impulse under the influences of both the gravity and the vertical rigid boundary. It is seen that v^* does not vary monotonically with ζ . When $\zeta > 0.008$, v^* decreases with increasing ζ . This is in general accordance with the previous literature (see Supponen *et al.* [1], where $0.004 < \zeta < 1$, and

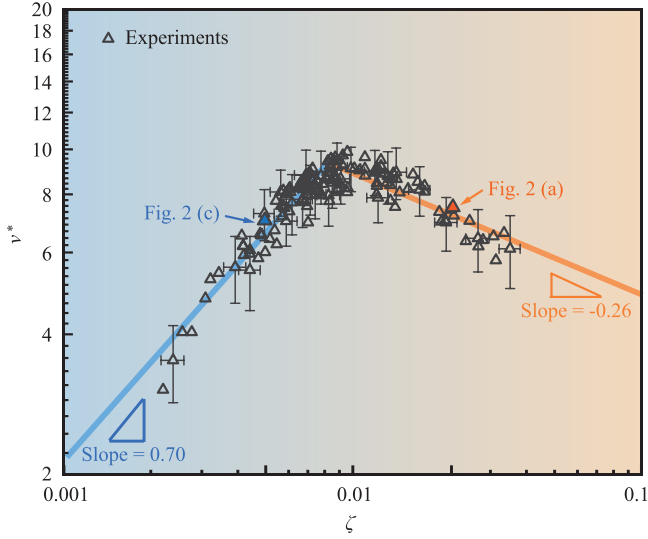


FIG. 4. Dependence of nondimensional jet velocity v^* on ζ . The particular cases with back illuminations illustrated in Figs. 2(a) and 2(c) are marked with orange and blue arrowheads, respectively. Some measurement uncertainties are shown by the error bars. The orange and blue lines indicating the slopes are derived from (5).

Zhang *et al.* [9], where $0.04 < \zeta < 0.25$). However, a significantly different dependence of v^* on ζ occurs when the parameter range expands to $\zeta < 0.008$. In this region, the velocity v^* increases with increasing ζ . Although such a transition has not been documented in previous studies, it can be partially understood if one notes that $\zeta = 0$ actually corresponds to a spherical bubble collapse with no jet ($v^* = 0$).

This particular scaling law of jet velocity v^* against ζ in Fig. 4 can also be further investigated by adopting the concept of Kelvin impulse. Recall that the Kelvin impulse is strongly correlated with the jet, in the sense that the presence of the former causes the bubble to deform and eventually become a multiconnected domain with a piercing jet while maintaining its impulse conserved [3]. In the process of jet formation, instead of the bubble collapsing uniformly to its center in all directions, a volume of liquid is pushed in the direction of the Kelvin impulse. For intermediate jets as in the present experiments, this process occurs mainly in a very short-time duration at the end of bubble collapses. Thus the integrated momentum variation across the bubble surface, which is the definition of the Kelvin impulse, can be roughly represented by the properties of the liquid volume as

$$\zeta = \Delta(m^* v^*) \propto r^{*3} v^*|_{t^*=1} - r^{*3} v^*|_{t^*=0}, \quad (4)$$

where m^* is the dimensionless form of the mass of the liquid volume driven by the Kelvin impulse until the bubble collapses, and r^* is the corresponding length scale of this part of the liquid. Here, $t^* = t/T_C$ is the dimensionless time of the bubble evolving, and $t^* = 0$ and $t^* = 1.0$ denote the generation and collapse moments of the bubble, respectively. If the bubble is considered a point source and its initial radius R_0 is small enough, the initial impulse $r^{*3} v^*|_{t^*=0}$ can be considered 0 [22]. Then (4) becomes $\zeta \propto r^{*3} v^*|_{t^*=1}$.

The length scale r is proportional to the bubble radius R when the bubble begins to deform, and is also closely related to the displacement of the bubble centroid. With the decreasing of ζ , the deformation of the bubble and the formation of the jet are delayed in the bubble life cycle. In the process of cavitation collapse, there is a finite minimum radius of the cavitation bubble, R_{\min} , because of the noncondensable gas in the cavitation bubble. Therefore, there exists a critical condition $\zeta = \zeta_c$, where the jet forms just when the bubble reaches the minimum radius R_{\min} . When $\zeta > \zeta_c$, the characteristic size of the liquid volume to form the jet r^* decreases with the decrease

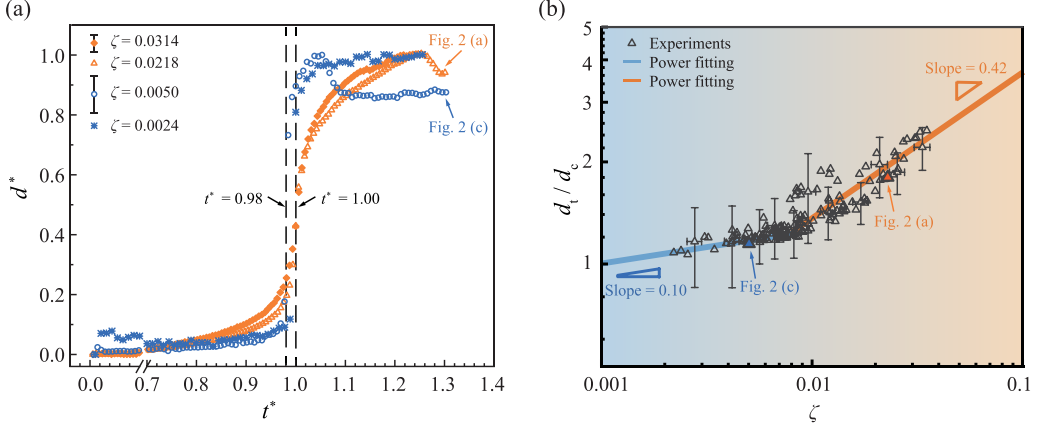


FIG. 5. Characteristics of the dimensionless displacement of the bubble center. The particular cases with back illuminations illustrated in Figs. 2(a) and 2(c) are marked with orange and blue arrowheads, respectively. (a) The displacement d^* during the growth and collapse of the bubble at different ζ . The uncertainty of d^* for each case is shown next to the corresponding legend. (b) The nondimensional length scale d_t/d_c against ζ . Some measurement uncertainties are shown by the error bars.

of ζ , while for $\zeta < \zeta_c$, due to the limitation of R_{\min} , r^* does not change significantly with ζ (in Appendix C, we give a schematics of the formation of jets with different anisotropic parameter ζ). It is difficult to define r^* directly in the experiments, but we find that the displacement characteristic of d_t/d_c can reflect the changing trend of r^* vs ζ .

The motion of the bubble center can have distinct features at different ζ , as shown in Fig. 5. The displacement of the bubble center d as it evolves can be normalized by the maximum displacement d_{\max} during its growth, collapse, and rebound as $d^* = d/d_{\max}$. Experimental d^* vs t^* characteristics are then exemplified in Fig. 5(a) with four typical cases, where $t^* = 1.0$ denotes the instance of the bubble collapse. Three consecutive stages of the motions of the bubble centers are identified for all cases. From the growth to the early stage of the collapse of the bubbles ($t^* < 0.7$), the bubble centers remain almost stationary. Then the most significant movements of the bubble centers occur when the bubbles collapse ($t^* \sim 1.0$), and the jets appear instantly. After that, the bubble centers have some residual displacements during the rebound. For cases with smaller ζ values ($\zeta = 0.0024$ and 0.0050 , marked with blue symbols), the sudden accelerations of the bubble centers are more concentrated in terms of the lasting time periods, than larger ζ values ($\zeta = 0.0218$ and 0.0314 , marked with orange symbols). It is also seen that in some cases, the thin vapor layer, or the vapor jet, collapses before the main body of the rebounding bubble, as indicated in Figs. 2(a) and 2(c). As a result, the displacement of the bubble decreases after the collapse of the vapor jet, as shown in Fig. 5(a).

To better express this difference, we plot d_t/d_c vs ζ in Fig. 5(b), where d_c is the instantaneous displacement of the bubble center at its collapse, and d_t is the total displacement of the bubble center during its life cycle from its generation to its first collapse (i.e., $t^* = 0-1.0$). In analysis, the value of d_c is evaluated by calculating the displacement during $t^* = 0.98-1.0$ with spline interpolation of the experimental readings. Although d_t/d_c increases with ζ in general, the dependence of d_t/d_c against ζ varies at $\zeta \sim 0.008$. When $\zeta < 0.008$, as seen in Fig. 5(a), since most of the acceleration of the bubble center occurs at the final collapse of the bubble (i.e., the jet forms near the minimum size of the bubble), d_t/d_c is close to 1 and follows $d_t/d_c \sim \zeta^{0.10}$ by a power fitting. When $\zeta > 0.008$, the influence of the Kelvin impulse becomes strong. The cavitation bubble deforms and the volume of the liquid is pushed before the bubble collapses to the minimum volume. Hence the displacement before the final bubble collapse accounts for a large proportion and the corresponding characteristic

jet size r^* is larger. In this region, d_t/d_c increases at $\sim \zeta^{0.42}$. Physically, we can think that d_t/d_c roughly reflects the radius of the bubble when the jet begins to form compared with its minimum radius. In addition, the experimental results show that $\zeta_c \approx 0.008$ is the critical condition where the jet starts to form when the cavitation bubble collapses to its minimum radius R_{\min} .

Note that the ratio d_t/d_c measures the nondimensional characteristic length scale of the liquid volume being pushed to form the jet at the bubble collapse. If we choose d_t/d_c as r^* and combine the above dependence of d_t/d_c against ζ , i.e., $d_t/d_c \propto \zeta^a$, with (4), we can readily derive that

$$v^* \propto \zeta^{1-3a} \approx \begin{cases} \zeta^{0.70}, & \zeta < 0.008, \\ \zeta^{-0.26}, & \zeta > 0.008. \end{cases} \quad (5)$$

The scaling law predicted by (5) is in good agreement with the experiments, as shown in Fig. 4. From the above discussions, it is seen that the different dependencies of v^* on ζ between $\zeta < 0.008$ and $\zeta > 0.008$ originate from the different collapsing behaviors of bubbles under pressure anisotropy, more specifically, the deformation and migration characteristics of bubbles during collapses. In this sense, $\zeta = 0.008$ here roughly distinguishes the strength of the effects of the Kelvin impulse in the present experiments.

V. CONCLUSIONS

In the present paper, we investigate the dynamics of a laser-induced buoyant bubble near a vertical rigid boundary, where two factors that induce pressure anisotropy, i.e., gravity and a nearby vertical boundary, act simultaneously on the bubble. The unique feature of this setup is that the main pressure gradients caused by the factors are perpendicular to each other. We focus on both the direction and strength of the inclined microjet generated at the nonspherical bubble collapse under the combined effects of the factors, characterized by the jet angle and the jet velocity, respectively.

For this purpose, systematic experiments are carried out in a sealed water tank with different combinations of the magnitudes of the two factors. By adjusting the background pressure p_∞ in the tank and correspondingly changing the maximum bubble radius R_{\max} , the influence of gravitational acceleration \mathbf{g} can be varied. Meanwhile, the standoff distance of the bubble against the solid boundary l_1 , or its nondimensional form $\gamma = \frac{l_1}{R_{\max}}$, is also controlled.

By adopting the concept of Kelvin impulse in its nondimensional form, the relative contributions of the vertical boundary and gravity to the time integral of the forces acting on the bubble surface during its growth and collapse can be estimated by two nondimensional vectors, $\zeta_w = -0.195\gamma^{-2}\frac{l_1}{l_1}$ and $\zeta_g = -\frac{\rho g R_{\max}}{\Delta p}$, respectively, where Δp is the pressure difference between the inside and outside of the bubble, and ρ is the liquid density. The jet direction is influenced by the combined effects and can be evaluated by the superposition of the two vectors, resulting in $\tan \theta = \zeta_g/\zeta_w$. This dependence is successfully validated against the experimental results. In addition, we discover that the boundary effect on the jet angle cannot be neglected in the present experimental setup, even when γ far exceeds the limit of influence when it was studied separately as described in the previous literature.

Within the current range of the parameter space, intermediate jets occur when the bubbles rebound, in terms of the shape and the occurrence instance of the jets. Considering this feature, the maximum jet velocity is characterized by the maximum migration velocity of the bubble centroid v . Then the nondimensional jet velocity $v^* = \frac{v}{\sqrt{\Delta p/\rho}}$ can be presented with respect to the combined factor $\zeta = \sqrt{\zeta_g^2 + \zeta_w^2}$. In this manner, a distinctive nonmonotonic dependence of v^* on ζ is revealed, where v^* increases with increasing ζ when $\zeta < 0.008$, while it decreases with increasing ζ when $\zeta > 0.008$. Next, we prove that by choosing the normalized displacement of the bubble center during its final collapse as the characteristic length r^* , this scaling law can be well predicted by reviewing the integrated momentum variation across the bubble surface. Here, $\zeta = 0.008$ roughly distinguishes the strength of the effects of the Kelvin impulse.

The results of this research provide additional information on the nonspherical cavitation bubble dynamics under the simultaneous influence of multiple factors. Nonetheless, further research is needed for wide ranges of the parameter space, to investigate the behaviors of different forms of jets at the bubble collapses.

ACKNOWLEDGMENTS

We gratefully acknowledge inspiring discussions with C. Sun and M. Farhat, technical support by Y. Guo, and the help from our research group. We acknowledge financial support from the National Natural Science Foundation of China (NSFC, No. 52076120 and No. 52079066), the State Key Laboratory of Hydrosience and Engineering (2019-KY-04, and sklhse-2020-E-03, sklhse-2020-E-05), the Creative Seed Fund of Shanxi Research Institute for Clean Energy, Tsinghua University, and the R&D Program of Beijing Municipal Education Commission (No. KM202211417011).

APPENDIX A: DYNAMICS OF A LASER-INDUCED CAVITATION BUBBLE GENERATED UNDER LOW PRESSURE

In the experiments, we generate large bubbles at low ambient pressure conditions. To assess if the collapse process of these bubbles can still be described by the classic Rayleigh equation, we have investigated several representative cases under varying pressure conditions, as depicted in Fig. 6. The evolution of normalized bubble radius $R^* = R/R_{\max}$ versus dimensionless time $T^* = T/0.5T_C$ under different background pressures p_∞ are compared with the Rayleigh solution, where $0.5T_C = 0.915R_{\max}\sqrt{\frac{\rho}{\Delta p}}$ is the Rayleigh time. It is seen that the collapsing process of the cavitation bubble is basically consistent with the Rayleigh solution. Only under the lowest experimental pressure $p_\infty = 8476$ Pa, does the collapsing time of the bubble deviate from the Rayleigh time by about 7%. When p_∞ rises to 10 111 Pa, the evolution of the bubble is in good agreement with the theoretical prediction of the Rayleigh solution.

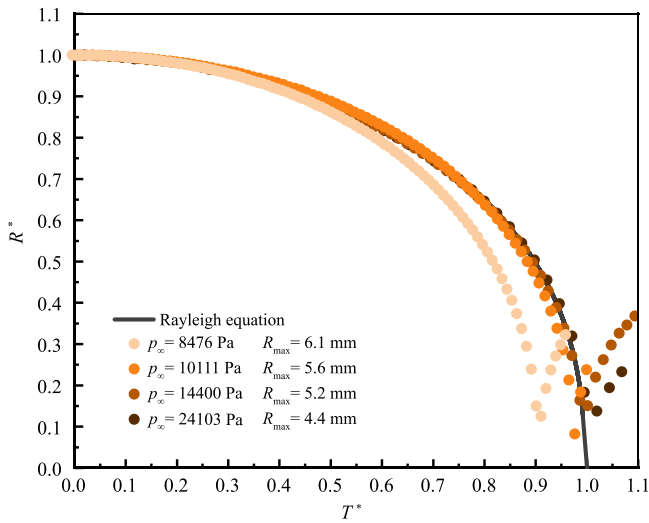


FIG. 6. The evolution of bubble radius R^* vs time T^* under different background pressures p_∞ compared with the Rayleigh equation.

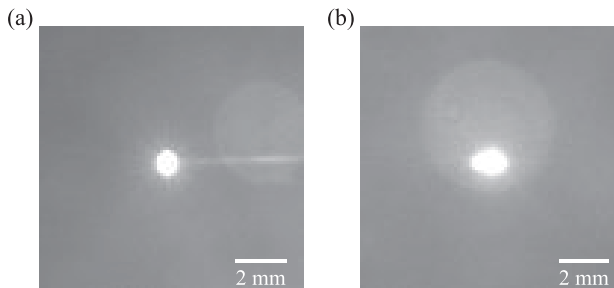


FIG. 7. The shape of the plasma in the water induced by (a) a vertically incident laser beam and (b) a horizontally incident laser beam. (Camera: Phantom V711; frame rate: 48 022 fps; exposure: 7 μ s; the convergent angle of the laser beam is about 40 $^\circ$.)

APPENDIX B: COMPARISON OF EXPERIMENTAL RESULTS WITH VERTICALLY AND HORIZONTALLY SHOT LASER BEAM

The direction and intensity of the microjet are very sensitive to the environment when the cavitation bubble collapses. To our knowledge, the sphericity of the cavitation bubble [25], the initial laser-induced shock waves [27], and other boundaries of the tank may all affect the final results. Since the microjet in the present study forms when the bubble size is very small, the flow-focusing effect caused by the tiny curvature radius would magnify the influence of any weak factors and more highly curved parts tend to reach a faster speed [25].

Besides the other boundaries in the tank, the initial laser-induced shock waves and their subsequent reflected shock waves might create additional impulses to the cavitation bubble. These additional impulses depend on the incident direction, the focus position of the laser, and the geometry of the tank. But these factors are difficult to quantify. Koukouvinis *et al.* [28] address in their paper that using a computational domain with the same cross section as the actual container is important to capture the correct collapse of a cavitation bubble when discussing a collapsing bubble subject to gravity.

On the other hand, gravity and the boundaries cause the cavitation bubble to deviate from a spherical shape, and the initial plasma created by the laser is not perfectly spherical, and is longer in the shooting direction of the laser, as shown in Fig. 7.

We also incorporated results with a vertically shot laser beam into the original data set with a horizontally shot laser beam, and present $\tan \theta$ vs ζ_g/ζ_w in Fig. 8, where jet angle θ is the angle between the jet and the horizontal directions. It is noteworthy that both sets of results demonstrate excellent linearity, but with different slopes. The disparities between them also vary at different ζ_g/ζ_w . Therefore, we may be able to formulate modified relationships between the jet angles and ζ_g/ζ_w in order to combine all the results.

As per prior discussions, the deviations between the two sets and the theoretical prediction can be attributed to the nonuniformly distributed bubble curvature, i.e., the bubble deformation. The diagram in Fig. 9 illustrates varieties of bubble deformation due to distinct factors. With a vertically shot laser beam, the bubble would elongate in the vertical direction, leading to a bigger jet angle. Conversely, if the laser is shot horizontally, or if the bubble is restricted by a vertical rigid wall, and is subject to gravity according to Supponen *et al.* [1], it would become elongated in the horizontal direction, resulting in a smaller jet angle.

Taking into account the above understanding, we define a shape factor f that incorporates the influence of various parameters on the sphericity of the bubble. Specifically, f is a function of the combined Kelvin impulse ζ (induced by gravity and the rigid wall), and the laser beam ζ_L , i.e., $f(\zeta, \zeta_L)$. The relationship between the jet angle θ and the ratio ζ_g/ζ_w considering the bubble deformation could be modified as $\tan \theta = f(\zeta, \zeta_L)\zeta_g/\zeta_w$. Based on the experimental results, we

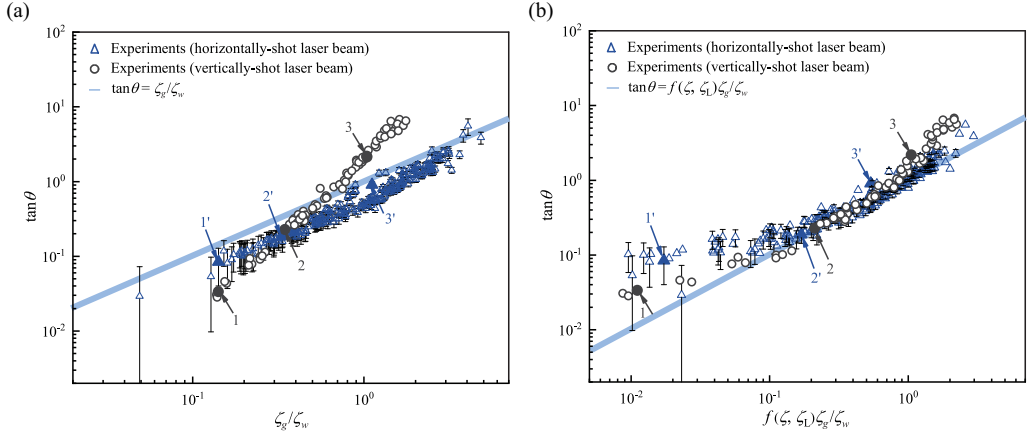


FIG. 8. Dependence of jet angle against functions of nondimensional Kelvin impulses. (a) $\tan \theta$ vs ζ_g/ζ_w . (b) $\tan \theta$ vs $f(\zeta, \zeta_L)\zeta_g/\zeta_w$.

construct the following functional form of f :

$$f = \begin{cases} \left(\frac{1-a(\zeta+\zeta_L)}{1+a(\zeta+\zeta_L)} \right)^b, & \text{horizontally shot laser,} \\ \left(\frac{1-a(\zeta-\zeta_L)}{1+a(\zeta-\zeta_L)} \right)^b, & \text{vertically shot laser,} \end{cases} \quad a > 0, \quad b > 0. \quad (\text{B1})$$

The function satisfies $f(0, 0) = 1$. The parameter $(\zeta \pm \zeta_L)$ captures the combined impact of the laser, rigid wall, and gravity. When the laser beam is fired horizontally, the deformation effects caused by all the factors stretch out horizontally and the parameter becomes $(\zeta + \zeta_L)$. On the other hand, when the laser beam is fired vertically, the deformation effects caused by the laser differ from those of the rigid wall and gravity and the parameter becomes $(\zeta - \zeta_L)$. Choosing $a = 20$, $b = 1.5$, and $\zeta_L = 0.003$ for the horizontally shot laser beam and $\zeta_L = 0.009$ for the vertically shot laser beam, the experimental results converge with one another and agree with the theoretical prediction, depicted in Fig. 8(b). In order to reduce the influence of the bottom wall when the laser is shot from the vertical direction, we use a convergent lens with a longer focal length (focal length = 50 and 70 mm for the horizontally and vertically shot laser beams, respectively), so different values of ζ_L are chosen for the two directions. It should be noted that when the jet angle is small, even minor measurement errors can be magnified in logarithmic coordinates, causing the deviation on the left-hand side in Fig. 8(b) to appear more prominent. Figure 10 presents high-speed images of typical cases highlighted in Fig. 8.

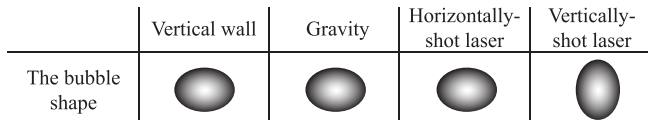


FIG. 9. Bubble deformations caused by different factors.

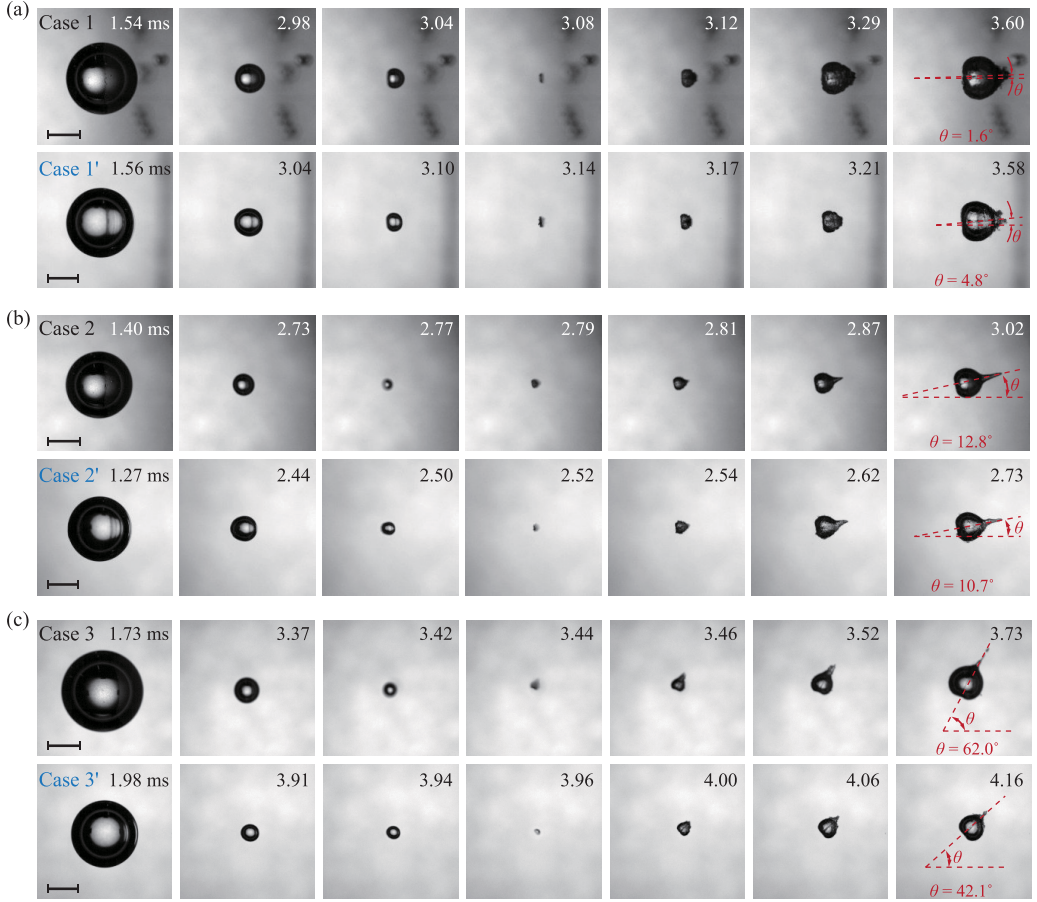


FIG. 10. Comparisons of the jet directions between experiments with vertically shot laser beam (cases 1, 2, 3) and horizontally shot laser beam (cases 1', 2', 3'), where $\zeta_g/\zeta_w \approx 0.14, 0.34, 1.11$ for (a)–(c), respectively. The scale bars in the figure are 5 mm. (Camera: Phantom V711; frame rate: 48 022 fps; exposure: 7 μ s.)

APPENDIX C: PHYSICAL PROCESS OF JET FORMATION UNDER DIFFERENT ANISOTROPIC PARAMETERS

Figure 11 gives a schematic plot of the collapsing process of the bubble under different ζ . The Kelvin impulse or anisotropy parameter ζ causes the bubble to deform, and the deformation subsequently develops into the microjet. Meanwhile, the deformation of the cavitation bubble leads to the migration of the bubble center. In another view, the Kelvin impulse pushes a volume of liquid around the bubble (the area enclosed by the red dotted line in Fig. 11) to get a faster collapsing speed and finally develop into a microjet. The characteristic length of the volume of liquid is r , which is proportional to the radius R when the bubble begins to deform and is also closely related to the displacement of the bubble centroid.

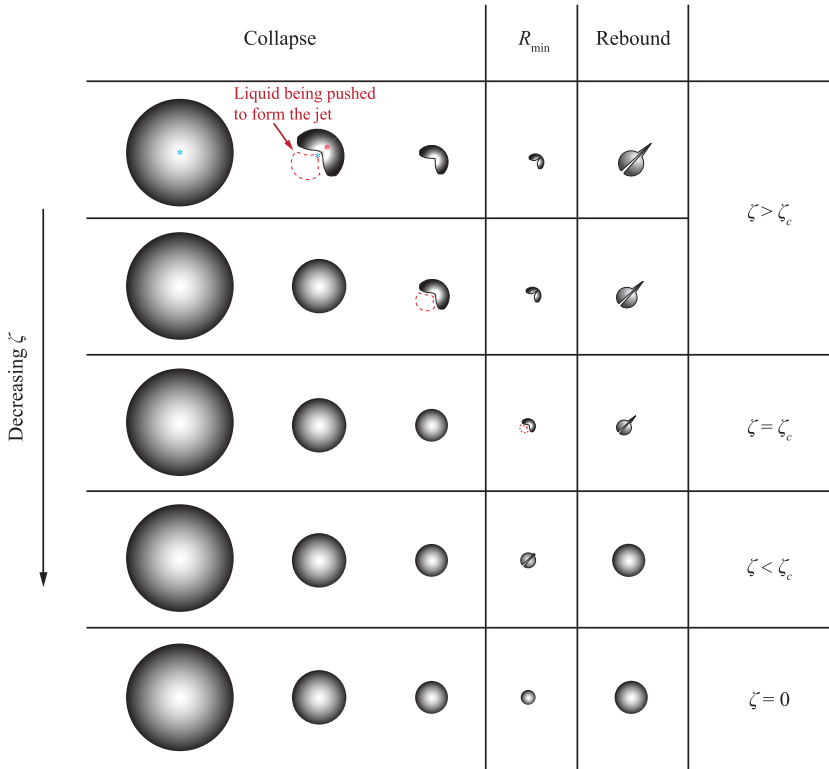


FIG. 11. Schematics of the formation of jets with different anisotropic parameters.

- [1] O. Supponen, D. Obreschkow, M. Tinguely, P. Kobel, N. Dorsaz, and M. Farhat, Scaling laws for jets of single cavitation bubbles, *J. Fluid Mech.* **802**, 263 (2016).
- [2] D. Obreschkow, M. Tinguely, N. Dorsaz, P. Kobel, A. de Bosset, and M. Farhat, Universal Scaling Law for Jets of Collapsing Bubbles, *Phys. Rev. Lett.* **107**, 204501 (2011).
- [3] T. B. Benjamin and A. T. Ellis, The collapse of cavitation bubbles and the pressures thereby produced against solid boundaries, *Philos. Trans. R. Soc. A* **260**, 221 (1966).
- [4] J. R. Blake and D. C. Gibson, Cavitation bubbles near boundaries, *Annu. Rev. Fluid Mech.* **19**, 99 (1987).
- [5] Y. X. Yang, Q. X. Wang, and T. S. Keat, Dynamic features of a laser-induced cavitation bubble near a solid boundary, *Ultrason. Sonochem.* **20**, 1098 (2013).
- [6] E. A. Brujan, T. Noda, A. Ishigami, T. Ogasawara, and H. Takahira, Dynamics of laser-induced cavitation bubbles near two perpendicular rigid walls, *J. Fluid Mech.* **841**, 28 (2018).
- [7] C. E. Brennen, *Hydrodynamics of Pumps* (Cambridge University Press, Cambridge, UK, 2011).
- [8] E. A. Brujan, A. Pearson, and J. R. Blake, Pulsating, buoyant bubbles close to a rigid boundary and near the null final Kelvin impulse state, *Int. J. Multiphase Flow* **31**, 302 (2005).
- [9] A. M. Zhang, P. Cui, J. Cui, and Q. X. Wang, Experimental study on bubble dynamics subject to buoyancy, *J. Fluid Mech.* **776**, 137 (2015).
- [10] Y. Tagawa and I. R. Peters, Bubble collapse and jet formation in corner geometries, *Phys. Rev. Fluids* **3**, 081601(R) (2018).
- [11] Q. X. Wang, M. Mahmud, J. Cui, W. R. Smith, and A. D. Wamsley, Numerical investigation of bubble dynamics at a corner, *Phys. Fluids* **32**, 053306 (2020).

- [12] J. P. Best, W. K. Soh, and C. F. Yu, An experimental investigation of buoyant transient cavity collapse near rigid cylindrical boundaries, *J. Fluids Eng.* **118**, 195 (1996).
- [13] Q. X. Wang, Numerical simulation of violent bubble motion, *Phys. Fluids* **16**, 1610 (2004).
- [14] M. Tinguely, The effect of pressure gradient on the collapse of cavitation bubbles in normal and reduced gravity, Ph.D. thesis, École Polytechnique Fédérale de Lausanne, 2013.
- [15] A. Kiyama, T. Shimazaki, J. M. Gordillo, and Y. Tagawa, Direction of the microjet produced by the collapse of a cavitation bubble located in a corner of a wall and a free surface, *Phys. Rev. Fluids* **6**, 083601 (2021).
- [16] See Supplemental Material at <http://link.aps.org/supplemental/10.1103/PhysRevFluids.8.083601> for high-speed videos of typical cases in Fig. 2.
- [17] O. Supponen, Collapse phenomena of deformed cavitation bubbles, Ph.D. thesis, École Polytechnique Fédérale de Lausanne, 2017.
- [18] J. C. Isselin, A.-P. Alloncle, and M. Autric, On laser induced single bubble near a solid boundary: Contribution to the understanding of erosion phenomena, *J. Appl. Phys.* **84**, 5766 (1998).
- [19] J. R. Blake, B. B. Taib, and G. Doherty, Transient cavities near boundaries. Part 1. Rigid boundary, *J. Fluid Mech.* **170**, 479 (1986).
- [20] J. P. Best and J. R. Blake, An estimate of the Kelvin impulse of a transient cavity, *J. Fluid Mech.* **261**, 75 (1994).
- [21] J. R. Blake, D. M. Leppinen, and Q. X. Wang, Cavitation and bubble dynamics: The Kelvin impulse and its applications, *Interface Focus* **5**, 20150017 (2015).
- [22] J. R. Blake, The Kelvin impulse: Application to cavitation bubble dynamics, *ANZIAM J.* **30**, 127 (1988).
- [23] J. R. Blake and P. Cerone, A note on the impulse due to a vapour bubble near a boundary, *J. Aust. Math. Soc. B* **23**, 383 (1982).
- [24] C. F. Hung and J. J. Hwangfu, Experimental study of the behaviour of mini-charge underwater explosion bubbles near different boundaries, *J. Fluid Mech.* **651**, 55 (2010).
- [25] C. Lechner, W. Lauterborn, M. Koch, and R. Mettin, Jet formation from bubbles near a solid boundary in a compressible liquid: Numerical study of distance dependence, *Phys. Rev. Fluids* **5**, 093604 (2020).
- [26] M. S. Plesset and R. B. Chapman, Collapse of an initially spherical vapour cavity in the neighbourhood of a solid boundary, *J. Fluid Mech.* **47**, 283 (1971).
- [27] Y. Tagawa, S. Yamamoto, K. Hayasaka, and M. Kameda, On pressure impulse of a laser-induced underwater shock wave, *J. Fluid Mech.* **808**, 5 (2016).
- [28] P. Koukouviniis, M. Gavaises, O. Supponen, and M. Farhat, Numerical simulation of a collapsing bubble subject to gravity, *Phys. Fluids* **28**, 032110 (2016).